IOPscience iopscience.iop.org

Home Search Collections Journals About Contact us My IOPscience

Crossover from quasi-static to dense flow regime in compressed frictional granular media

This content has been downloaded from IOPscience. Please scroll down to see the full text.

2013 EPL 104 46001

(http://iopscience.iop.org/0295-5075/104/4/46001)

View the table of contents for this issue, or go to the journal homepage for more

Download details:

IP Address: 193.48.255.141
This content was downloaded on 18/12/2013 at 08:48

Please note that terms and conditions apply.

A Letters Journal Exploring
the Frontiers of Physics

November 2013

EPL, **104** (2013) 46001
doi: `10.1209/0295-5075/104/46001`

`www.epljournal.org`

Crossover from quasi-static to dense flow regime in compressed frictional granular media

F. Gimbert[1,3], D. Amitrano[1] and J. Weiss[2]

[1] *Institut des Sciences de la Terre, CNRS-Université Joseph Fourier, Grenoble - 1381 rue de la Piscine, BP 53, 38041 Grenoble Cedex 9, France*
[2] *Laboratoire de Glaciologie et de Géophysique de l'Environnement, CNRS-Université Joseph Fourier, Grenoble 54 rue Moliere, BP 96, F-38402 Saint-Martin d'Hères Cedex, France*
[3] *Seismological Laboratory, California Institute of Technology - 1200 E. California Blvd., Pasadena, CA 91125, USA*[(a)]

received 6 May 2013; accepted in final form 15 November 2013
published online 10 December 2013

PACS `62.20.-x` – Mechanical properties of solids
PACS `64.60.De` – Statistical mechanics of model systems (Ising model, Potts model, field-theory models, Monte Carlo techniques, etc.)
PACS `91.60.Ba` – Elasticity, fracture, and flow

Abstract – Being ubiquitous in a large variety of geomaterials, granular assemblies play a crucial role in the mechanical stability of engineering and geophysical structures. For these applications, an accurate knowledge of the processes at the origin of shear localization, *i.e.* faulting, in frictional granular assemblies submitted to compressive loading is needed. Here we tackle this problem by performing discrete-element numerical simulations. A thorough analysis of the evolution of multi-scale mechanical properties as approaching sample macroscopic instability is performed. Spatial correlations operating within the shear stress and strain fields are analyzed by means of a coarse-graining analysis. The divergence of correlation lengths is reported on both shear stress and strain fields as approaching the transition to sample instability. We thus show that the crossover from a quasi-static regime where the sample deforms infinitely slowly to a dense flow regime, where inertial forces play a significant role, can be interpreted as a critical phase transition. At this transition, no shear band of characteristic thickness can be defined.

Copyright © EPLA, 2013

Introduction. – The mechanical behavior of granular materials is of wide concern, from natural hazard to engineering applications. However, the evolution of properties towards the flowing instability is still partially understood. For assemblies of non-frictional, hard (non-deformable) and spherical particles submitted to a macroscopic shear stress, the concept of jamming [1] provides a powerful framework to understand the onset of granular flow. Force chains, *i.e.* heterogeneous distributions of contact forces on a scale much larger than the typical particle size, allow assemblies of non-frictional particles to exhibit jammed states [2]. These jammed states correspond to assemblies resisting small stresses without irreversible deformation, *i.e.* to assemblies that exhibit a macroscopic friction inherited from cooperative effects, whereas unjammed states are associated to irreversible flow under any applied shear [3,4]. The jamming transition for such spheres is controlled by the critical packing fraction ϕ [1].

Here we investigate the transition of granular assemblies toward macroscopic instability in a different situation. Elastically deformable and frictional disks are loaded under multi-axial compression. This compressive loading situation is relevant when studying geophysical instabilities such as the mechanics of granular gouges within fault zones or the dynamics of landslides. In the 2-dimensional configuration we consider, multi-axial loading consists in increasing the axial stress σ_1 while keeping the radial stress σ_3, *i.e.* the confining pressure, constant (see fig. 1). Doing so allows sample shearing, as the deviatoric stress $\tau = \sigma_1 - \sigma_3$ is continuously increased.

The differences between this configuration and classical ones used to study jamming [1] are twofold. First, in assemblies of frictional grains, the parameter that controls whether the grain assembly behaves as a jammed or an unjammed state is the fraction of grains that carry forces, named non-rattler grains, rather than the packing fraction [5]. Second, instead of keeping the sample volume constant during mechanical testing, the

---

[(a)] Present address.

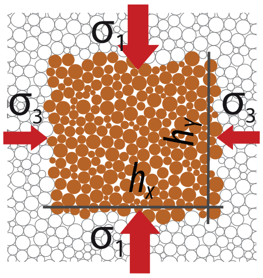

Fig. 1: (Color online) Multi-axial loading configuration on a sample made of 225 grains. Empty circles correspond to sample replication.

compressive loading conditions considered here involve a confining pressure that prevents the non-rattler-grain fraction from evolving freely. As a consequence, a percolating strong force network remains in the flowing phase, called the dense flow regime [6].

To investigate the behavior of geomaterials at the approach of macroscopic instability under these compressive multi-axial conditions, laboratory experiments have been previously conducted on either continuous rocks [7,8] and discrete materials such as sand [9] or synthetic analogous media [10]. In continuous materials, the bifurcation theory has been widely used to describe the macroscopic instability. This theory considers a transition from homogeneous to heterogeneous deformation materialized by the creation of a perennial macroscopic shear band of characteristic thickness, spanning the whole sample [11,12]. Within granular materials, either in experiments [9] or in simulations [13], deformation fields computed over large macroscopic strain windows in the vicinity of macroscopic instability also show perennial shear bands, with a possible characteristic size. On the other hand, by considering relatively small temporal scales under similar loading configurations, other studies report heterogeneous and long-range correlated kinematics of quasi-static granular flow [14,15]. At which temporal and spatial scales and at which stage of the loading does the granular assembly deform homogeneously? What are the relevant key features of the stress and strain fields associated to the onset of macroscopic instability? Here we investigate this problem using numerical simulations. We thoroughly quantify the heterogeneity of stress and strain fields at the approach of the transition from a quasi-static regime, where the sample resists to the applied stress by deforming infinitely slowly, to a dense flow regime, where inertia comes into play.

Simulation setting. – The numerical simulations we conduct use the molecular-dynamics discrete element method [16]. Two-dimensional granular assemblies of a number N_g of frictional circular grains are considered. To characterize sample size effects [17], 320 simulations with $N_g = 2500$, 80 simulations with $N_g = 10000$ and 20 simulations with $N_g = 45000$ have been performed. The results presented here concern 10000 grains samples. The grains areas are uniformly distributed. The largest grain diameter D_{max} is set such that $D_{max} = 3D_{min}$. Grains interact via linear elastic laws and Coulomb friction when they are in contact [18]. The normal contact force f_n is proportional to contact interpenetration δ via $f_n = k_n \times \delta$, where k_n is the normal contact stiffness coefficient. The tangential component f_t of the contact force is proportional to the tangential elastic relative displacement, with a tangential stiffness coefficient $k_t = k_n$. Neither cohesion nor rolling resistance is considered at grain contacts. The Coulomb condition $|f_t| \leq \mu_{micro} f_n$, where μ_{micro} is the grain friction coefficient, requires an incremental evaluation of f_t every time step, which leads to some amount of slip each time one of the equalities $f_t = \pm\mu_{micro} f_n$ is reached. A normal viscous component opposing the relative normal motion of any pair of grains in contact is also added to the elastic force f_n to obtain a damping of the dynamics.

The simulation procedure is divided into two steps. First, the granular assembly is built by performing an isotropic compression of dilute frictionless grains sets. This method builds dense and highly coordinated initial packings, characterized by a packing density of $\phi_i \approx 0.85$ and a backbone coordination number of $z_i^* = 4$, where z_i^* is expressed as $z_i^* = 2N_c/(N_g(1 - x_0))$ [19], N_c being the total number of contacts and x_0 the fraction of rattlers grains. Second, multi-axial compression tests are conducted using $\mu_{micro} = 1$. We perform the external mechanical loading on the grain assembly by using periodic boundary conditions [16]. A rectangular, periodic, simulation cell is defined by writing the linear operator $\mathbf{h}$ as $\mathbf{h} = \begin{pmatrix} h_x & 0 \\ 0 & h_y \end{pmatrix}$, where h_x and h_y correspond to the size of the cell period in the radial and axial direction (see fig. 1). Then, stresses are applied solving for the dynamic equations of motion of $\mathbf{h}$ by ensuring that the internal stresses computed over the whole grain assembly following eq. (1) (see below) are equal to the prescribed external stresses σ_1 and σ_3. We increase the axial stress σ_1 at constant rate by imposing a stress increment $\delta\sigma_1^{t_r}$ at each discretization time interval $t_r = \sqrt{\frac{m_{min}}{k_n}}/25$, where m_{min} is the mass of the lightest grain. This stress control loading mode avoids stress relaxations and associated feedbacks that would be obtained under strain-controlled loading, *i.e.* adjusting $\delta\sigma_1^{t_r}$ in order to axially deform at constant rate $\dot{\epsilon}_1$, where ϵ_1 is the axial deformation. In this stress-controlled case, stress and strain localization structures develop freely. We keep the confining pressure σ_3 as constant and sized by setting the contact stiffness $\kappa = k_n/\sigma_3$ equal to 1000 [16]. While chosen relatively low to ensure moderate computational times, this value of contact stiffness remains relevant for applications in geophysics and engineering mechanics. Within the Earth's crust, wave speeds [20] suggest κ-values of approximately 10^3 from hundreds of meters to several kilometers depth. Moreover, compression experiments performed on

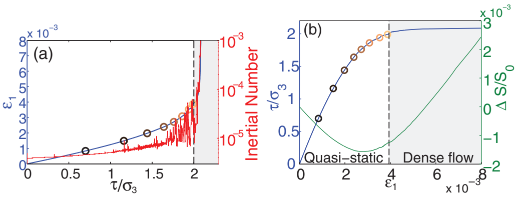

Fig. 2: (Color online) Macroscopic response of a 10000 grains sample compressed at constant stress rate $\delta\sigma_1^{tr} = 1.10^{-6}\sigma_3$. The inertial number I and the sample surface variation $\Delta S/S_0$ are defined in the main text. Color dots correspond to color lines in figs. 4 (top) and 5 (top). Dashed lines indicate the limit between quasi-static and dense flow deformation regimes.

assemblies of glass beads of approximate Young's modulus $E = 70$ GPa submitted to 100 kPa of confining pressure lead to a κ-value of 700.

Results. –

Macroscopic behaviour. Figure 2 shows the macroscopic response of a granular sample loaded using $\delta\sigma_1^{tr} = 1.10^{-6}\sigma_3$. The inertial number I quantifies the ratio between inertial forces and imposed forces and is defined as $I = \dot{\epsilon}_1\sqrt{\overline{m}/\sigma_3}$ [16], where $\overline{m}$ is the average grain mass. Initially, I is of the order of 10^{-6}–10^{-5} (see fig. 2(a)). As τ increases towards $2\sigma_3$, while undergoing fluctuations associated to plastic events, I remains lower than 10^{-4}, which is often considered an upper bound for quasi-static conditions [16,21]. Hence, in the range $0 \leq \tau < 2\sigma_3$, the sample undergoes quasi-static deformation. At values of τ larger than $\tau_c \approx 2\sigma_3$, I increases by several orders of magnitudes, reaching values of about 10^{-3}–10^{-2}. This drastic change in I-values defines the macroscopic instability and the transition to a dense flow regime, where inertial forces become significant. Figure 2(b) shows the surface change of the granular assembly $\Delta S/S_0 = \frac{(h_x h_y)_1 - (h_x h_y)_0}{(h_x h_y)_0}$, where 0 and 1 denote the initial and current configuration. Sample contraction is observed in the early stages of mechanical testing and essentially results from contacts elasticity, as it would not be observed in the limit of rigid grains [22]. Sample dilation irreversibly occurs after the maximum contraction and the dense flow transition observed at $\tau_c \approx 2\sigma_3$ occurs at packing fractions larger than the initial one.

The critical shear stress value $\tau_c \approx 2\sigma_3$ materializes the softening of the granular assembly, as it corresponds to a macroscopic friction coefficient of $\mu_{macro} \approx 0.5$ that is significantly smaller than the friction $\mu_{micro} = 1$ considered at the grain scale. While macroscopic hardening can be associated to the non-zero macroscopic friction obtained for an assembly of frictionless circular particles submitted to a similar compressional loading [3], the assemblies of frictional particles herein considered show a reverse behaviour, characterized by macroscopic softening. In the present configuration, collective effects and structural rearrangements generate weak zones whose spatial extent that are much larger than the particle size grows towards the macroscopic instability. Inelastic deformation and flow concentrate within these weak zones, resulting in a macroscopic softening. The quantification of these effects towards the macroscopic instability through the analysis of stress and strain fields is the backbone of this manuscript.

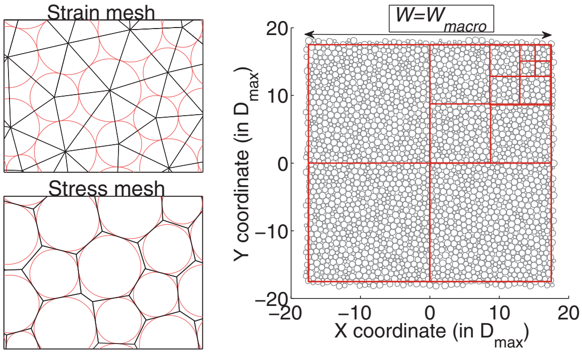

Fig. 3: (Color online) Left: Delaunay (top) and modified Voronoi (bottom) tesselations for a polydisperse granular material. Right: coarse-graining analysis on a 2500 grains sample.

Multi-scale analysis. We first characterize the stress field by quantifying the spatial extent of stress concentration regions using a coarse-graining analysis [23,24]. An average shear stress rate $\langle\dot{\tau}\rangle$ (see footnote [1]) is computed at different stages of mechanical testing (cf. color dots in fig. 2) over a time window T and over a broad range of spatial scales L, ranging from the micro-scale corresponding to mesh size (see fig. 3 (left)), to the macro-scale corresponding to sample size. Subsystems of the granular assembly are selected by defining square boxes of size W (see fig. 3 (right)). Grains are considered to belong to a given subsystem if their mass centers are included in the box of size W. For a given box of size W, the actual area spanned by the mesh associated to the selected grains assembly slightly differs from the area of the box W^2. This difference is due to the irregularity of the contour of the mesh at the boundary of the domain. Thus, for a set of N_{box} boxes of size W, we define the average scale L as $L = \frac{1}{N_{box}}\sum_{k=1}^{N_{box}} L_k$, where L_k is the scale associated to the box number k, computed as the square root of the sum of mesh element surfaces. The smallest subsystem of average size $L = 1.1D_{max}$ shows a maximum standard deviation of L_k-values of $0.2D_{max}$ for the Voronoi triangulation used to compute stresses and of $0.13D_{max}$ for the Delaunay triangulation used to compute strains (see fig. 3). No overlap of scales L_k occurs through successive values of W. For a given assembly of grains included in the box number k, the stress tensor is computed over all contacts carried by each grain using [25], *i.e.* writing

$$\sigma_{ij}^k = \frac{1}{L_k^2}\sum_{g_k}\sum_{c_k}(r_i^{c_k} - r_i^{g_k})f_j^{g_k c_k}, \qquad (1)$$

---

[1] The invariant x, where x represents τ for the shear stress or γ for the shear strain, is computed as $x = x_I - x_{II}$, where x_I and x_{II} are the principal components of the stress or strain tensor.

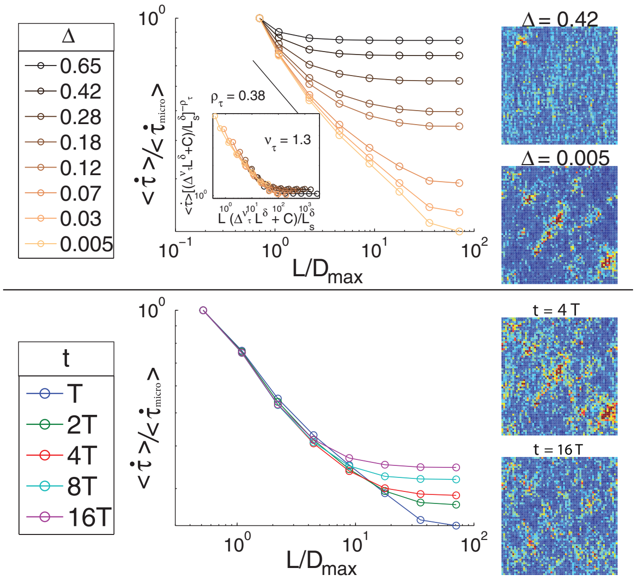

Fig. 4: (Color online) Multi-scale analysis performed on the shear stress rate field $\dot{\tau}$. A selection of corresponding fields is shown on the right side: an arbitrary color scale (not shown) has been chosen for each snapshot. Top: $\langle\dot{\tau}\rangle$ *vs.* L for decreasing values of Δ. Configuration locations on the stress-strain curve are shown in fig. 2. The timescale T is used to compute values of $\langle\dot{\tau}\rangle$. The inset displays data collapse with respect to Δ (eq. (2)). We find $\nu_\tau = 1.3$, $C = 0.5$ and $\delta = 1$. Bottom: $\langle\dot{\tau}\rangle$ *vs.* L at $\Delta = 0.005$ when increasing the timescale t from $t = T$ to $t = 16T$. For graphical convenience, all computed values have been normalized by the ones computed at the micro-scale.

where $f_j^{g_k c_k}$ is the j-th component of the contact force exerted on grain g_k at contact c_k, $r_i^{c_k}$ is the i-th component of the position vector of c_k, and $r_i^{g_k}$ is the i-th component of the position vector of the mass center of grain g_k. The stress rate tensor is obtained by differentiating the stress tensor components calculated at two successive configurations. These successive configurations are selected in time and separated one from the other by a time interval $T = \sqrt{N_g} \times 100 \times t_r$ that corresponds to the travel time of elastic waves through the whole sample [17].

Figure 4 (top) shows the results of the multiscale analysis performed on the stress rate field from the early stages of biaxial testing up to $\tau_c \approx 2\sigma_3$. Curves are selected with respect to the control parameter Δ defined as $\Delta = \frac{\tau_c - \tau}{\tau_c}$. At the early stages of macroscopic deformation, *i.e.* at large values of Δ, and at small spatial scales, $\langle\dot{\tau}\rangle$ decreases as L increases. Moreover, for L-values larger than a crossover scale l_τ^*, $\langle\dot{\tau}\rangle$ remains constant. We conclude that associated shear stress rate fields are heterogeneous for $l \ll l_\tau^*$ and homogeneous for $l \gg l_\tau^*$. Associated fields provided on the right-hand side of fig. 4 illustrate the connection between l_τ^* and the size of spatial zones of stress concentration. For $\Delta = 0.42$, the stress rate field shows a roughly homogeneous pattern at large spatial scales, *i.e.* scales larger than $l_\tau^* \approx 3D_{max}$ in that case, while the region of stress localization observed on the top-left part of the snapshot exhibits a spatial extent of the order of $l_\tau^* \approx 3D_{max}$ that corresponds to the crossover scale of the associated curve. We interpret l_τ^* as the correlation length [24]. As macroscopic deformation proceeds, l_τ^* grows until reaching the size of the system at τ_c. At that point, a power law scaling $\langle\dot{\tau}\rangle \sim L^{-\rho_\tau}$ is observed over the entire scale range, with $\rho_\tau = 0.38$. We verified using various sample sizes that the cut-off remaining on the scaling at $\Delta \to 0$ is a finite-size effect [17]. At $\tau = \tau_c$, large and strongly localized structures characterize the shear stress rate field (see snapshot at $\Delta = 0.005$). These scalings suggest a progressive structuring of the stress rate field as approaching the transition to the dense flow regime. We report an associated divergence of the correlation length l_τ^* by performing a collapse analysis (inset of fig. 4 (top)) and formulating that $l^* = l_\tau^*$ diverges as

$$l^* \sim \frac{L_s^\delta}{\Delta^\nu L_s^\delta + C}, \tag{2}$$

where L_s is the square root of the sample area and $\nu = \nu_\tau = 1.3 \pm 0.1$ is the exponent of divergence. The parameters δ and C characterize the finite-size effect [17]. The divergence of $l_\tau^* \sim \Delta^{-\nu_\tau}$ at $\Delta \to 0$ is confirmed from a similar analysis performed on other moments $\langle\dot{\tau}^q\rangle$ of the shear rate [17], revealing the multi-fractality of the shear rate field at the critical point. These particular features of the shear stress rate field are only observed at the specific timescale $t = T$, that corresponds to the travel time of elastic waves. At increasing timescales, *i.e.* for $t > T$, the departure from the power law scaling observed in fig. 4 (bottom) denotes a progressive homogenization of the shear stress rate field, materialized by the decrease of l_τ^* as t increases (see also the associated snapshots). We interpret the multi-scale properties of the shear stress rate field observed at $t = T$ to be associated to stress concentration events occurring simultaneously to the propagation of elastic information throughout the sample, which operates by means of elastic waves. The loss of scaling properties reported beyond this time, *i.e.* for $t > T$, implies that the multi-scale localization structures observed at $t = T$ have little memory, limited to the travel time of an elastic wave. In other words, the loss of scaling properties at $t > T$ is explained by the superposition of several stress concentration events operating at $t = T$, but uncorrelated in time one with the successive other.

We then investigate whether similar features characterize the shear strain field. A Delaunay triangulation is performed on the grain centers of the non-rattler-grains set (fig. 3). The partial derivatives are computed at the mesh scale as $\epsilon_{ij} = 1/2(\partial u_i/\partial x_j + \partial u_j/\partial x_i)$, where (u_1, u_2) and (x_1, x_2) are, respectively, the incremental displacements and spatial coordinates of grain centers. By averaging the partial derivatives, an average value of the shear strain rate is computed at increasing spatial scales L using the coarse-graining analysis exposed previously. Using the constant timescale $t = T$ to compute displacement rates, the correlation length associated to the shear

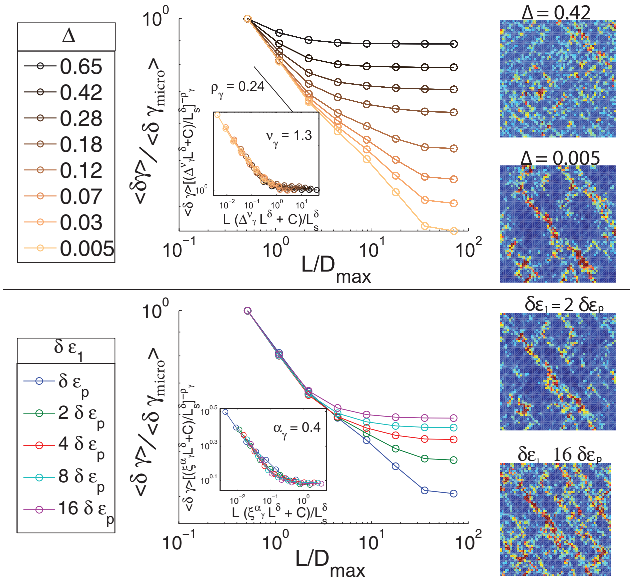

Fig. 5: (Color online) Multi-scale analysis performed on the incremental shear strain field $\delta\gamma$. A selection of corresponding fields is shown on the right side: an arbitrary color scale (not shown) has been chosen for each snapshot. Top: $\langle\delta\gamma\rangle$ *vs.* L for decreasing values of Δ towards the critical point. The deformation scale $\delta\epsilon_1 = \delta\epsilon_p = 1.10^{-5}$ is used to compute values of $\langle\delta\gamma\rangle$. The inset displays data collapse with respect to Δ (eq. (2)). We find $\nu_\gamma = 1.3$, $C = 0.5$ and $\delta = 1$. Bottom: $\langle\delta\gamma\rangle$ *vs.* L at $\Delta = 0.005$ when increasing $\delta\epsilon_1$ from $\delta\epsilon_1 = \delta\epsilon_p$ to $\delta\epsilon_1 = 32\delta\epsilon_p$. The inset displays data collapse with respect to $\xi = \frac{\delta\epsilon_1 - \delta\epsilon_p}{\delta\epsilon_p}$ (eq. (3)). We find $\alpha_\gamma = 0.4$. For graphical convenience, all computed values have been normalized by the ones computed at the micro-scale.

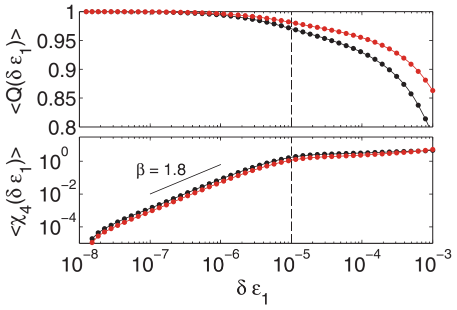

Fig. 6: (Color online) Susceptibility analysis performed in the quasi-static region on the sliding contacts belonging to the major (red curves) and minor (black curves) network. The vertical dashed line indicates the deformation value $\delta\epsilon_p = 1.10^{-5}$.

strain rate field does not diverge as approaching the transition to the dense flow regime (not shown). Thus, the structure of the strain rate field does not form simultaneously in time with the stress rate field, which would be the case if one considered only the elastic component of the strain. Here, for $N_g = 10000$, approximately 10^4 stress increments are prescribed during the propagation time of an elastic wave throughout the sample. Hence, a multitude of contacts, in our case about 5% of the whole contact network, are sliding although elastic information does not have time to travel across the entire sample. However, a progressive structuring of the shear strain field is observed when computing the scaling of the incremental shear strain $\langle\delta\gamma\rangle$ for constant macroscopic deformation windows $\delta\epsilon_1 = \delta\epsilon_p = 1.10^{-5}$. The divergence of the correlation length l^*_γ as approaching the transition to the dense flow regime is reported on the incremental shear strain field in fig. 5. This divergence is similar to the one observed on the shear stress rate field, as we find $\nu_\gamma = \nu_\tau = 1.3$ (eq. (2)). For larger macroscopic deformation windows $\delta\epsilon_1 > \delta\epsilon_p$, the deformation field no longer exhibits multi-scale properties and l^*_γ continuously decreases as $\delta\epsilon_1$ increases. This observation is in agreement with the study of [14], who reported a narrowing of the fluctuation velocity distributions at increasing timescales. As the material softens when τ increases (see fig. 2(a)), the time of integration associated to the constant deformation window $\delta\epsilon_1 = \delta\epsilon_p$ decreases when approaching the dense flow transition. This time can be either smaller or larger than the travel time T of an elastic wave, depending on the imposed loading rate $\delta\sigma_1^{tr}$. All the presented scalings are indifferently obtained for loading rate values $\delta\sigma_1^{tr}$ smaller than $\delta\sigma_1^{tr} = 1.10^{-6}$. For larger values of $\delta\sigma_1^{tr}$, the divergence of the correlation length is no longer observed [17]. In that case, the mechanical behavior of the granular assembly is related to a dense flow regime from the initial stages of deformation, attesting that the scalings reported in this study are associated to the transition from quasi-static to dense flow regimes of deformation. Interestingly, $\delta\epsilon_1 = \delta\epsilon_p$ remains equal to 1.10^{-5} whatever the loading rate considered, suggesting that a given, constant, amount of plastic activity has to operate in order to observe multi-scale properties within the incremental shear strain field.

To better understand the role of plastic activity in setting the characteristic value $\delta\epsilon_p$, we perform a four-point dynamic susceptibility χ_4 analysis on the inter-particles contact network [26,27]. From an "initial" contact configuration selected at an axial deformation ϵ_1^{init}, we compute the self-overlap order parameter $Q_{\epsilon_1^{init}}(\delta\epsilon_1) = \frac{1}{N_c}\sum_{i=1}^{N_c} w_i$, where N_c is the number of the non-sliding contacts of the initial configuration and w_i is a step-function cutoff that equals 1 if no sliding event occurred at contact i over the deformation window $\epsilon_1^{init} \rightarrow \epsilon_1^{init} + \delta\epsilon_1$, and 0 otherwise. The first two moments $Q(\delta\epsilon_1) = \langle Q_{\epsilon_1^{init}}(\delta\epsilon_1)\rangle$ and $\chi_4(\delta\epsilon_1) = N_c[\langle Q_{\epsilon_1^{init}}(\delta\epsilon_1)^2\rangle - \langle Q_{\epsilon_1^{init}}(\delta\epsilon_1)\rangle^2]$ of $Q_{\epsilon_1^{init}}(\delta\epsilon_1)$ (calculated from sample-to-sample fluctuations) are computed for initial configurations selected at the previously used Δ-values, *i.e.* within the quasi-static region ($\tau < \tau_c$). This analysis evaluates the number and the associated spatial heterogeneity of sliding events that occur as the axial deformation increases. As no significant variations of $Q(\delta\epsilon_1)$ and $\chi_4(\delta\epsilon_1)$ are observed with respect to Δ, fig. 6 shows the average functions $\langle Q(\delta\epsilon_1)\rangle$ and $\langle\chi_4(\delta\epsilon_1)\rangle$ computed over all the values of Δ. Major and minor force networks, defined by selecting contact forces larger and smaller than the average force, are considered separately. By construction, $\langle Q(\delta\epsilon_1)\rangle$ is initially equal to 1. As $\delta\epsilon_1$ increases, $\langle Q(\delta\epsilon_1)\rangle$ decreases but never reaches 0, as about 35% (respectively, 55%) of the contacts of the minor (respectively, major) network never slide. These non-sliding contacts associated to the remaining rigid bodies illustrate the localization of permanent deformation. At low values of $\delta\epsilon_1$, $\langle\chi_4(\delta\epsilon_1)\rangle$ increases as $\langle\chi_4(\delta\epsilon_1)\rangle \sim \delta\epsilon_1^\beta$ with $\beta = 1.8$. This increase results from the nucleation of spatially correlated events of contact sliding. As $\delta\epsilon_1$ exceeds the threshold value $\delta\epsilon_p = 1.10^{-5}$, $\langle\chi_4(\delta\epsilon_1)\rangle$ saturates. Thus, at $\delta\epsilon_p = 1.10^{-5}$, *i.e.* when multi-scale properties are observed on the shear deformation field (see fig. 5), all the spatially correlated contacts located close to the Coulomb criterion, *i.e.* susceptible to slide, have been destabilized. At this stage, only 4% (respectively, 3%) of contacts have slid in the minor (respectively major) network.

Conclusion. – We have shown that, in dense granular assemblies, stress and strain fields are both characterized by a growing correlation length that diverges as approaching the onset of macroscopic instability. This instability can therefore be identified as a critical point. A similar behavior has recently been reported in compressive failure of continuous materials [24,28]. Herein, this behavior is observed as long as the macroscopic instability is reached in the quasi-static regime. On the reverse, the critical behaviour is no longer observed for imposed loading rates large enough so that the inertial number is larger than 10^{-4} before the instability [17]. We interpret these stress and strain specific structures as resulting from dynamic stress redistributions induced by the local dissipation of elastic energy, materialized by contact sliding. These features can only be observed for characteristic timescales for stresses, and characteristic macroscopic strain increments for strains. These characteristic timescales may be sensitive to varying initial packing properties, such as, for example, low coordinated and/or loose initial samples. This sensitivity has not been investigated in this study.

The last question that arises is whether a limit in decreasing correlation length l_γ^* is reached at $\Delta \to 0$ for values of $\delta\epsilon_1$ much larger than $\delta\epsilon_p$. If so, this limit value observed on the shear strain field would characterize the thickness of a perennial macroscopic shear band potentially formed at the onset of instability. We hypothesize that, close to the critical point ($\Delta \to 0$), l_γ^* varies as

$$l_\gamma^* \sim \frac{L_s^\delta}{L_s^\delta \Pi^{\alpha_\gamma} + C}, \tag{3}$$

where $\Pi = \frac{\delta\epsilon_1 - \delta\epsilon_p}{\delta\epsilon_p}$ and α_γ is the exponent of divergence with respect to Π. This hypothesis is tested from a collapse analysis (inset of fig. 5). We find $\alpha_\gamma = 0.4$, meaning that l_γ^* keeps decreasing as the considered deformation window size $\delta\epsilon_1$ increases. Thus, no intrinsic scale of saturation, potentially associated to a shear band thickness, is identified at the onset of macroscopic instability.

* * *

We thank Gaël Combe for providing the DEM code and for fruitful discussions. We thank Jean Braun for providing routines to compute Voronoi tesselations. All computations were performed at SCCI-CIMENT Grenoble.

REFERENCES

[1] Liu A. and Nagel S., *Nature*, **396** (1998) 21.
[2] Cates M. E., Wittmer J. P., Bouchaud J. P. and Claudin P., *Phys. Rev. Lett.*, **81** (1998) 9.
[3] Combe G. and Roux J.-N., *Phys. Rev. Lett.*, **85** (2000) 3628.
[4] Lespiat R., Cohen-Addad S. and Hölher R., *Phys. Rev. Lett.*, **106** (2011) 148302.
[5] Bi D., Zhang J., Chakraborty B. and Berhinger R. P., *Nature*, **480** (2011) 355.
[6] Pouliquen O. and Chevoir F., *C. R. Phys.*, **3** (2002) 163.
[7] Mogi K., *J. Geophys. Res.*, **72** (1967) 5117.
[8] Haimson B. and Chang C., *Int. J. Rock Mech. Min. Sci.*, **17** (2000) 285.
[9] Desrues J. and Viggiani G., *Int. J. Numer. Anal. Meth. Geomech.*, **28** (2004) 279.
[10] Hall S. A., Wood D. M., Ibraim E. and Viggiani G., *Granular Matter*, **12** (2010) 1.
[11] Rudnicki J. W. and Rice J. R., *J. Mech. Phys. Solids*, **23** (1975) 371.
[12] Haimson B. C. and Rudnicki J. W., *J. Struct. Geol.*, **32** (2010) 1701.
[13] Tordesillas A., *Philos. Mag.*, **87** (2007) 32.
[14] Radjai F. and Roux S., *Phys. Rev. Lett.*, **89** (2002) 064302.
[15] Richefeu V., Combe G. and Viggiani G., *Geotech. Lett.*, **2** (2012) 113.
[16] Radjai F. and Dubois F., *Discrete Numerical Modeling of Granular Materials* (Wiley-ISTE) 2011.
[17] See supplementary material at `http://isterre.fr/annuaire/pages-web-du-personnel/florent-gimbert/article/publications`.
[18] Cundall P. A. and Strack O. D. L., *Géotechnique*, **29** (1979) 47.
[19] Agnolin I. and Roux J.-N., *Phys. Rev. E*, **76** (2007) 6.
[20] Brocher T. M., *Bull. Seismol. Soc. Am.*, **98** (2008) 2.
[21] MiDi GDR, *Eur. Phys. J. E*, **14** (2004) 341.
[22] Combe G. and Roux J.-N., in *Deformation Characteristics of Geomaterials, 3me Symposium sur le Comportement des Sols et des Roches Tendres, Lyon, 22–24 Septembre 2003*, edited by di Benedetto H. *et al.* (Swets & Zeitlinger, Lisse) 2003, p. 1071.
[23] Marsan D., Stern H., Lindsay R. and Weiss J., *Phys. Rev. Lett.*, **93** (2004) 178501.
[24] Girard L., Amitrano D. and Weiss J., *J. Stat. Mech.*, (2010) P01013.
[25] DeGiuli E. and McElwaine J., *Phys. Rev. E*, **84** (2011) 041310.
[26] Abate A. R. and Durian D. J., *Phys. Rev. E*, **76** (2007) 021306.
[27] Keys A. S., Abate A. R., Glotzer S. C., and Durian D. J., *Nat. Phys.*, **3** (2007) 260.
[28] Girard L., Weiss J. and Amitrano D., *Phys. Rev. Lett.*, **108** (2012) 225502.